



# Analysis of the integrated characteristics of the CPS (combined power system) of a bottoming organic Rankine cycle and a diesel engine



Chen Yue\*, Dong Han, Wenhao Pu

College of Energy and Power Engineering, Jiangsu Province Key Laboratory of Aerospace Power Systems, Nanjing University of Aeronautics and Astronautics, No. 29 Yudao Street, Jiangsu Province, Nanjing City 210016, People's Republic of China

## ARTICLE INFO

### Article history:

Received 17 September 2012

Received in revised form

19 May 2014

Accepted 30 May 2014

Available online 25 June 2014

### Keywords:

Engine

Organic Rankine cycle

Waste heat recovery

Integration characteristics

## ABSTRACT

This study analyses the integrated characteristics of a CPS (combined power system) consisting of a topping diesel engine and a bottoming ORC (organic Rankine cycle). Two models (an integrated and a cascaded CPS model) for the same CPS have been developed based on the experimental data. The results show that the process of integrating the ORC causes a substantial decrease in the power output of the ICE subsystem, this integration outweighs the corresponding power output increasing from the ORC subsystem, and the overall thermal efficiency of the integrated CPS model is higher than that of the standalone ICE system model but lower than that of the cascaded CPS model, which can be determined from the pressure drop on the exhaust gas side of the ORC evaporator and is reflected in the overall thermodynamic performance. Moreover, the matching characteristics of the heat-transfer and fluid flow conditions in a fixed sized evaporator are analysed in the integrated CPS model. The results show that when the intake airflow rate decreases, the temperature of the exhaust gas exiting the evaporator decreases to the minimum allowed temperature, which is below the dew point, and this low-temperature might cause corrosion problems in the subsequent components.

© 2014 Elsevier Ltd. All rights reserved.

## 1. Introduction

The ICE (internal combustion engine) is the primary power production device in use today due to its high power density and efficiency. The average thermal efficiencies of spark ignition ICE and compression ignition ICEs are approximately 1/3 [1]. According to the second law of thermodynamics, the thermal efficiency of the ICE is near its maximum value, and any further improvements will not exceed 45% thermal efficiency using the current ICE standalone ICE cycle. Approximately two-third of the thermal energy is emitted into the environment as waste heat, i.e., via the exhaust gas, the coolant and the lubricating oil [2,3], and nearly 40% of the heat energy is wasted through the exhaust gas [4]. In recent years, national energy security, escalating energy prices, rising liquid fuel consumption and stringent environmental emission regulations have become the primary driving force in the search for sustainable and economically viable technologies for efficient and clean approaches to ICE energy conversion and utilisation [5]. Many waste heat recovery technologies have been proposed to increase ICE

thermal efficiency. Yamada et al. [6] proposed a novel waste heat recovery schematic for hydrogen ICE. Kalyan et al. [7] proposed the use of an ORC (organic Rankine cycle) to recover heat from a dual-fuel engine. Shu et al. [8] analysed the thermodynamic performance of a thermoelectric-generator-based waste heat recovery technologies. Vaja et al. [9] conducted a thermodynamic analysis of an ICE-ORC system based on several organic working fluids to show its characteristic efficiency matching. Fang et al. [10] reviewed several conventional waste technologies, e.g., mechanical turbo-compounding, electrical turbo-compounding, Rankine cycle and thermoelectric generation, and studied an electric turbo-compounding technology in detail. Among these technologies, ORC shows great potential for waste heat recovery [6,9]. ORC can be used to convert low-grade thermal energy into useful work through the selection of appropriate working fluids. The coupling of a bottoming ORC with a topping ICE is a promising application that allows for the utilisation of the wasted heat from the ICE and the realisation of a CPS (combined power system) unit with increased overall thermal efficiency. Because the ORC system generates additional power without consuming extra fuel, the specific pollutant emissions of the CPS can be reduced.

Recently, many highly efficient bottoming ORCs with ICEs have been reported. The research results showed that the waste heat

\* Corresponding author. Tel./fax: +86 25 8489 2270/25 8489 2201.

E-mail addresses: [yuechen025@gmail.com](mailto:yuechen025@gmail.com), [yuechen@nuaa.edu.cn](mailto:yuechen@nuaa.edu.cn) (C. Yue).

**Nomenclature**

$A$	area, m <sup>2</sup>
$B_c$	Baffle cut, %
$B_s$	Baffle space, mm
$c_{p,a}$	constant pressure specific heat of the air, kJ/(kg K)
$c_{p,g}$	constant pressure specific heat of the exhaust gas, kJ/(kg K)
$c_{p,R}$	constant pressure specific heat of the dichlorotrifluoroethane vapour, kJ/(kg K)
$c_{p,cf}$	constant pressure specific heat of the coolant, kJ/(kg K)
$d$	diameter, m
$E_x$	exergy, kW
$f_i$	interfacial friction factor
$f_r$	fraction coefficient
$h$	specific enthalpy, kJ/kg
$h_{tot}$	overall heat-transfer coefficient in evaporator, kW/(m <sup>2</sup> K)
$j_b$	correction factor for bundle and pass partition bypass streams
$j_c$	correction factor for Baffle configuration
$j_{id}$	correction factor for any adverse temperature gradient build up in laminar flows
$j_l$	correction factor for baffle leakage
$j_s$	correction factor for large baffle spacing at the inlet and outlet sections
$k$	compound heat-transfer coefficient, kW/(m <sup>2</sup> K)
$k_a$	specific heat ratio of air
$k_g$	specific heat ratio of the exhaust gas
$l$	length, m
$m$	mass flow rate, kg/s
$m_{a0}$	air flow rate at rated load
$M$	molar mass, kg/kmol
$n$	rotation speed, rps
$n_0$	revolution speed of the engine at rated load
$N_{ob}$	number of baffle
$N_b$	number of tubes
$N_c$	number of cylinders
$p$	pressure, kPa
$P$	power output, kW
$Pr$	Prandtl number
$q_{LHV}$	lower heating value of the fuel, kJ/kg
$Q_1$	heat added during combustion stroke, kW
$Q_2$	waste heat recovered, kW
$Q_3$	exhaust waste heat, kW
$Q_4$	discharged heat of the condenser, kW
$R$	fouling resistances, m <sup>2</sup> K/kW
$R_a$	Specific gas constant of the air, kJ/(kg K)
$Re$	Reynolds number
$R_g$	specific gas constant of the exhaust gas, kJ/(kg K)
$S_i$	spacing at the inlet, mm
$T$	temperature, K
$t_{ps}$	tube passes
$t_{pt}$	tube pattern
$V$	volume/volume flow rate
$w$	specific work, kW/kg
$W$	power output, kW
$x$	fuel molar flow rate, kmol/s
$y$	air molar flow rate, kmol/s
$z$	adiabatic or isentropic exponent through turbine

**Symbols**

$\beta$	expand ratio during isentropic expansion stroke
$\gamma$	temperature ratio during constant-volume heating
$\Delta\eta$	improvement of efficiency, %

$\Delta T$	temperature difference, K
$\Delta p$	pressure difference, kPa
$\eta$	efficiency, %
$\lambda$	conductive coefficient, kW/(m K)
$\mu$	viscosity, Pa s
$\pi$	circular constant, 3.1416
$\rho$	density, kg/m <sup>3</sup>
$\tau$	number of crank revolutions
$\varphi$	viscosity correction fraction

**Subscripts**

0,1,2...	state point
1c	constant-volume combustion
1p	isobaric combustion
a	air
B	bore
c	cold-side/condensation
cf	cooling fluid
com	compressor of turbocharger
combustion	combustion stroke of engine
compression	compression stroke of engine
CPS	combined power system
cross	cross-section area
cl	clearance volume of the cylinder
disp	cylinder displacement volume
e	evaporation
eq	equivalent
ex	exergy efficiency
expansion	expansion stroke of the engine
exhaust	exhaust process of the engine
fuel	fuel
g	exhaust gas
i	inner of tube/intercooler outlet
itb	turbine of turbocharger
ICE	internal combustion engine
Intake	intake process of engine
LMTD	log mean temperature difference
MEP	mean effective pressure
net	net work
o	outer of tube
ORC	organic Rankine cycle
p	Pressure
pump	pumping gases process
Pit	pitch
p_ORC	pump in ORC
R	organic working fluid
s	inner of shell
so	outer of shell
s_m	average value at shell-side
S	stroke
t	the tube-side of the evaporator
t_m	average value at tube-side
to	turbine reference point
t,o	outer of the tube bundle
t_ORC	turbine in ORC
v	volume/vapor

**Abbreviations**

CPS	combined power system
IAF	intake air flow rate
ICE	internal combustion engine
MEP	mean effective pressure
ORC	organic Rankine cycle
RPS	revolutions per second

from the ICEs could be efficiently recovered using the ORC and that the overall thermal efficiency of the system could be increased significantly. He et al. [11] investigated the thermal performance of an ICE-ORC CPS and found that its maximum thermal efficiency was improved by 21% compared with that of a standalone ICE system when all three types of waste heat (i.e., cooling water, exhaust gas and lubricating oil) are recovered. Wang et al. [12] proposed a novel system combining a gasoline engine with a dual loop ORC to recover the exhaust heat from the ICE. Their research results showed that the absolute effective thermal efficiency of the ICE was improved by 3% to 6% throughout the engine's operational region.

During the evaluation of the overall thermal performances of the ICE-ORC CPS, many researchers noted that the systematic influence of the ORC on the ICE thermal performances must be determined. Domingues et al. [13] performed a systematical assessment of the RC (Rankine cycle) vehicle exhaust waste heat recovery potential in three operating conditions, and an efficient steam RC schematic was recommended. Stobart [14] analysed the influence of the evaporation pressure on the heat-transfer characteristics. The results showed that the higher evaporating pressure allowed for an increase in the first and second law efficiencies of the ORC and reduced the temperature differences across the heat exchanger surfaces, additionally, the heat-transfer rates decreased significantly. Tian et al. [15] studied the influence of the fluids selection in the ORC subsystem on the overall power output performance of the ICE-ORC CPS.

In addition to the above, the addition of a bottoming ORC subsystem to the recovery of waste heat from an ICE is not simply an addition of a cascaded thermal energy recovery and conversion unit; the operation of the bottoming ORC affects the operating parameters and thermal performance of the topping ICE subsystem in several ways. First, when a malfunction occurs, and the ORC subsystem is not able to work, the waste heat from the coolant and lubricating oil cannot be removed in time. As a result, the performance of the topping ICE thermodynamic cycle decreases and eventually ceases to work altogether. Second, the heat-transfer resistance of the exhaust gas is much greater than that of the organic working fluid in the evaporator. Therefore, if only the ICE exhaust gas waste heat is recovered by the ORC subsystem on the exhaust gas side of the evaporator, then the overall heat-transfer coefficient of the evaporator will be low. Additionally, the effective heat-transfer area of the evaporator is large, thus the corresponding pressure loss on the exhaust gas side of the evaporator is large. That is, the pressure loss must match the heat transferred in the evaporator of the ORC subsystem [16,17]. An evaporator that can be used to manage the heat load (and is of a reasonable size) without excessive pressure drop was of great importance, especially for ICE waste heat recovery applications. Mavridou et al. [16] studied heat-transfer and pressure drop matching characteristics based five evaporator configurations. The results showed an intrinsic pressure drop in the evaporator caused by the heat-transfer that cannot be avoided. When enhanced heat-transfer measures are performed on the exhaust gas side, the pressure loss on the exhaust gas side of the evaporator is increased [17]. To discharge the exhaust gas from the exhaust devices and stop the refluxing of ambient air, the operational parameters of the engine exhaust manifold must be adjusted. Therefore, the ICE power output, the ORC power output and the overall thermal performance of the CPS are influenced [18]. However, a thorough and comprehensive investigation of the matching characteristics of the ICE-ORC CPS has not yet been performed.

In this paper, we present an updated design for an integrated ICE-ORC CPS in which the ORC subsystem is located in the bottom cycle to recover the exhaust gas waste heat from the topping ICE thermodynamic cycle. In the evaporator of the ORC subsystem, the pressure drop required to match the heat-transfer on the exhaust

gas side is calculated, and measurements of the adjusted engine mean effective pressure (MEP) are adopted to evaluate the integrated thermodynamic performance. The operational parameters and waste heat quantities are collected using experimental data from a commercial CAT3516CDITA ICE at different loads [19]. Dichlorotrifluoroethane (R123) is selected as the working fluid in the ORC subsystem. The standalone ICE power system and the cascaded ICE-ORC CPS without calculating the pressure drop on the exhaust gas side of the evaporator are used as the basis for comparison to show the potential thermal performance improvement of the integrated ICE-ORC CPS at different engine loads.

## 2. The ICE-ORC CPS description

The thermal process of the ICE-ORC CPS analysed in this study is shown in Fig. 1. The temperature–entropy diagram of the process is shown in Fig. 1(b).  $T_0$ ,  $T_i$ ,  $T_e$  and  $T_c$  represent the ambient temperature, intercooler outlet temperature, evaporation temperature and condensation temperature in ORC subsystem, respectively.

Compared with the waste heat from the coolant and the cooling lubricating oil, the exhaust gas is held a higher exergy. Additionally, the ICE is capable of working even if the bottoming ORC subsystem, which recovers waste heat from exhaust gas ceases to work, in this case, only the waste heat from the exhaust gas will be recovered by the ORC subsystem. To save significant work in the modification of existing ICEs and cooling subsystems, the evaporator for the ORC subsystem is placed downstream. Moreover, the temperature of the exhaust gas exiting the evaporator decreases as the flow rate of the exhaust gas decreases, which is helpful for reducing the exhaust gas flow noise of the muffler and reducing the size of the muffler in the exhaust unit. Two types of working fluids are used in the ORC subsystem. The isentropic fluid dichlorotrifluoroethane is selected as the working fluid in this study due to its preferred performance versus that of other organic working fluids when recovering waste heat from low-temperature exhaust gas [20]. A mixed coolant of MEG (mono ethylene glycol) and water (50% MEG and 50% water) is used to cool the condenser of the ORC subsystem [21], which is the same as that used in the engine radiator and is placed at the same location as the ambient air cooling subsystem. In the driveline subsystem, the overall power output of the ICE subsystem and the ORC subsystem is converted by the driving gear equipment.

The evaporator is not only used as a waste heat regenerator but is also used to couple the ICE subsystem with the ORC subsystem in this study. As shown in the temperature–entropy diagram of Fig. 1(b), the pressure drop on the exhaust gas side is accompanied by the waste heat recovery of the evaporator, which causes the engine exhaust manifold pressure and its corresponding thermal performance to increase. In this study, a horizontal shell-tube evaporator is selected for use in the ORC subsystem. The hot exhaust gas flows through the shell-side of the evaporator, and dichlorotrifluoroethane is heated and evaporated on the tube-side of the evaporator. Dichlorotrifluoroethane is condensed by the mixed liquid coolant in the condenser of the ORC subsystem. In contrast to the conventional, ideal diesel cycle, the actual combustion process in a diesel engine involves constant-volume combustion and constant pressure combustion. As shown in Fig. 1(a), ambient air is compressed by the compressor of the turbocharger (0–1), isobarically cooled in the intercooler (1–i) and then sent to the intake end of the ICE. The working principles in the cylinders of the ICE are similar to those of the traditional ICE thermodynamic cycles (i–2–3–4–5). The compression process of the intake air in cylinder (i–2) is adiabatic and reversible, the combustion process is divided into two stages: constant-volume combustion (2–3) and isobaric combustion (3–4). It should be noted that some

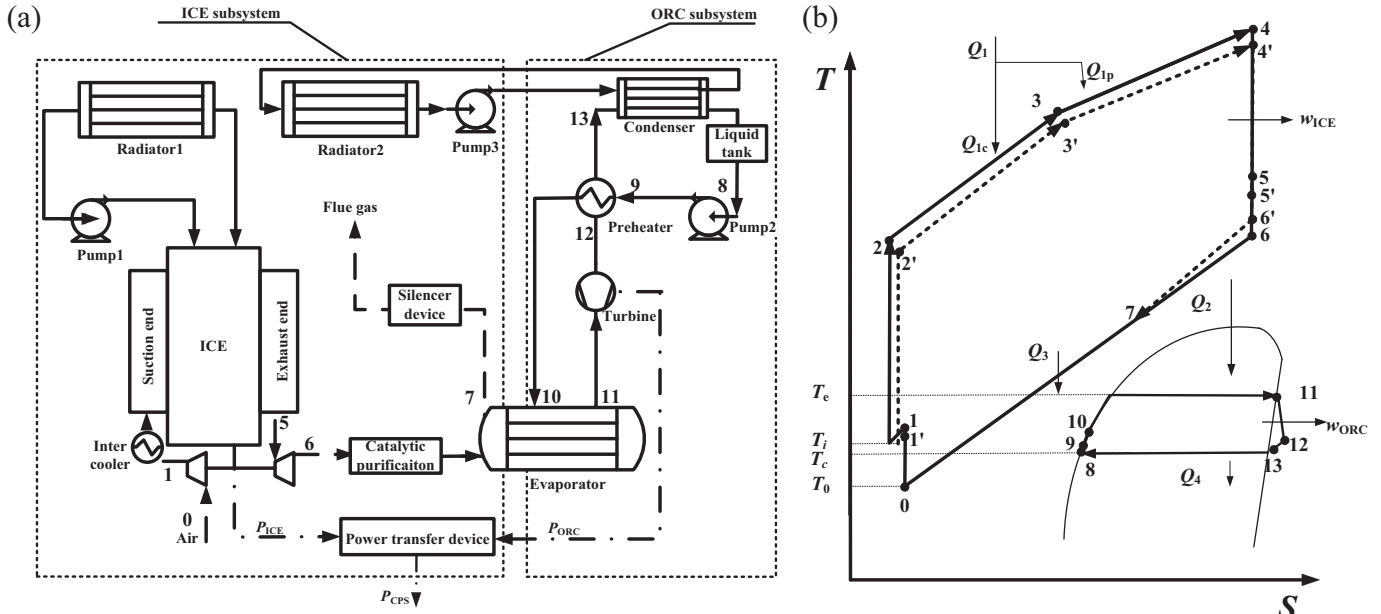


Fig. 1. The thermal process of the ICE-ORC CPS: (a) flow diagram, and (b) temperature–entropy diagram.

mechanical work is generated during the isobaric combustion stage (3–4). The expansion process is isentropic (4–5). The exhaust gas exits the ICE exhaust port (5) and expands into the turbine of the turbocharger (5–6), where the waste heat of the exhaust gas is converted into power and drives the compressor in the turbocharger. The exhaust gas exiting the turbocharger is cooled in the evaporator (6–7), and dichlorotrifluoroethane is simultaneously heated and evaporated in the evaporator (10–11). The dichlorotrifluoroethane is a dry organic working fluid; it changes to a gas after expansion (11–12), like other dry organic working fluids [9,22]. Therefore, a preheater is placed in the ORC subsystem to recover some of the heat of the dichlorotrifluoroethane vapour exiting the turbine (12–13), and the cold liquid dichlorotrifluoroethane is heated (9–10). In Fig. 1(a),  $P_{ICE}$  and  $P_{ORC}$  represent the power output in the ICE subsystem and the ORC subsystem, respectively.

As shown in Fig. 1(b), the ideal operational processes of the ICE subsystem in the cascaded ICE-ORC CPS model are indicated by the solid line in Fig. 1(b). Only the heat-transfer process in the evaporator is calculated (6–7), and the influence of the fluid pressure drop in evaporator is omitted ( $p_6 - p_6$ ). The actual waste heat recovery process in the integrated ICE-ORC CPS model must match the pressure loss in the evaporator of the ICE-ORC CPS, which causes the pressure to drop correspondingly ( $p_6 - p_6$ ). To discharge the exhaust gas from the exhaust unit and avoid the refluxing of ambient air, the actual operational pressure in the turbine is adjusted from 6 to 6', and the actual cooling process on the exhaust gas side of the evaporator is 6'–7. To match the turbine of the turbocharger, the compressor outlet of the turbochargers is adjusted from 1 to 1', and the actual operational processes in the ICE are indicated by the dashed line (1'–2'–3'–4'–5') in Fig. 1(b).

As shown in Fig. 1(b),  $Q_1$  refers to the lower heating value of the fuel introduced to the ICE subsystem,  $Q_2$  and  $Q_3$  represent the waste heat recovered in the evaporator and the exhaust heat discharged to the atmosphere, respectively, and  $Q_4$  is the waste heat from the condensed organic working fluid discharged to atmosphere from the condenser of the ORC subsystem.  $w_{ICE}$  and  $w_{ORC}$  are the specific work of the ICE subsystem and ORC subsystem, respectively.

### 3. The mathematical model

#### 3.1. Problem statement

This paper focuses on the performance of the integrated ICE-ORC CPS considering the influences of the evaporator size and operational condition. Two mathematical models are developed to establish several configurations including the standalone ICE system and ICE-ORC CPS.

The flow diagram calculations of the different ICE-ORC CPS models are shown in Fig. 2. Fig. 2(a) represents the cascaded CPS model, and Fig. 2(b) represents the actual integrated CPS model. Because the calculation procedure for the standalone ICE system model is similar to that of the ICE subsystem model in the cascaded CPS model, the details of the model calculation for the standalone ICE system are not introduced here.

First, the proposed model shown in Fig. 2(a) is used to calculate the thermodynamic performance of the standalone ICE system. The simulation problem assumes the ambient conditions, air flow rate, fuel flow rate, the size of the cylinders, mean effective pressure, the clearance of the cylinder, intake pressure and exhaust gas temperature are known; the initial value of the temperature ratio in the constant-volume combustion stroke,  $\gamma$ , and expansion ratio during the expansion stroke,  $\beta$ , are assigned. The control variables of the model are  $\gamma$  and  $\beta$ ; these variables are defined in Section 3.3 in detail. The power output of the ICE system is calculated using the mathematical model and verified using the experimental data.

Then, the proposed model, shown in Fig. 2(a), is used to calculate the cascaded CPS model. Based on the standalone ICE system results for  $\gamma$  and  $\beta$ , the evaporating pressure, condensing pressure, and size of the evaporator are given. The heat-transfer coefficients of the evaporator and the maximum waste heat recovered are calculated according to the flow patterns and operational states of the exhaust gas and the organic working fluid. The overall power output and thermal efficiency of the cascaded ICE-ORC CPS, without calculating the evaporator pressure drop, the influence of the bottoming ORC on the top ICE is determined.

Finally, the proposed model shown in Fig. 2(b) is used to calculate the thermodynamic performance of the integrated CPS

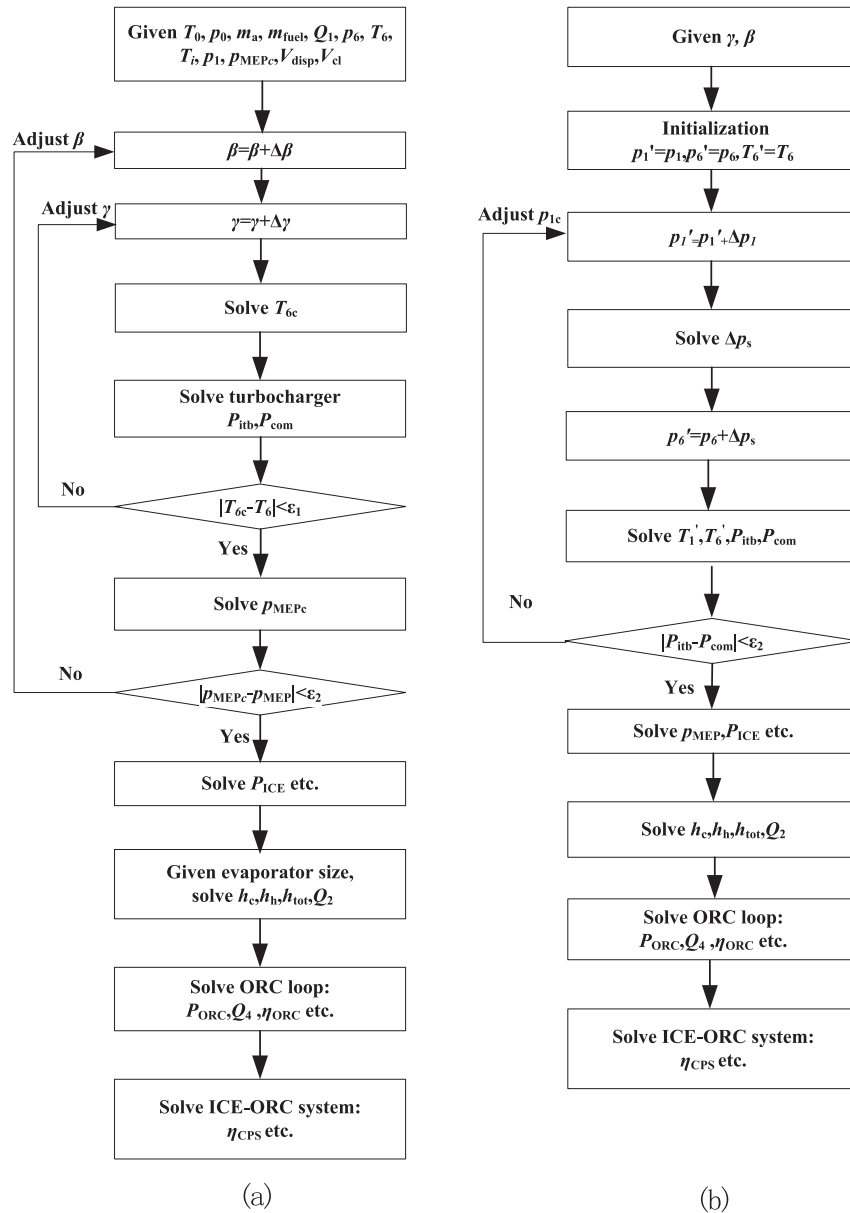


Fig. 2. The calculation flow diagram (a) the cascaded ICE-ORC CPS model; and (b) the integrated ICE-ORC CPS model.

considering the influence of the bottoming ORC on the topping ICE. In contrast to the cascaded CPS model, both the heat-transfer coefficient and the pressure drop on the exhaust gas side of the evaporator are calculated in the integrated CPS model. In particular, the influence of the pressure drop on the exhaust gas side on the adjustment of the operational state of the turbocharger and the ICE thermodynamic cycle performance in the ICE subsystem are studied. The overall power output is solved, and the integrated thermodynamic performance of the ICE-ORC CPS is analysed.

### 3.2. Assumptions

The following are the main assumptions used to derive the mathematical models.

- The system operates at steady-state conditions.
- The non-equilibrium allowance is omitted.
- The pressure drops in the evaporator and condenser of the ORC loop are omitted.

### 3.3. The ICE subsystem

#### 3.3.1. The ICE thermodynamic cycle calculation model

For a complete analysis of the ICE thermodynamic cycle, the concept of mean effective pressure (MEP) is used. The MEP is a fictitious constant pressure acting on the piston during the power stroke that would generate the net work in the cycle ( $W_{net}$ ) as the piston sweeps out the displacement volume in a single expansion ( $V_{disp}$ ). The MEP is calculated using the following expression:

$$p_{MEP} = \frac{W_{net}}{V_{disp}} \quad (1)$$

Because pMEP is formulated as the network of the ICE thermodynamic cycle, it can be split into the various work terms of each of the stroke [23]. Thus,

$$W_{\text{net}} = -W_{\text{compression}} + W_{\text{combustion}} + W_{\text{expansion}} - \text{abs}(W_{\text{exhaust}} - W_{\text{intake}}) \quad (2)$$

The work performed in the adiabatic compression stroke (1–2) is

$$W_{\text{compression}} = \rho_i \cdot V_{\text{disp}} \cdot c_{p_a} \cdot T_i \cdot \left( \left( \frac{p_2}{p_i} \right)^{\frac{k_a-1}{k_a}} - 1 \right) / \eta_{\text{compression}} \quad (3)$$

The work done by the cylinder gas on the piston during exhaust is

$$W_{\text{exhaust}} = p_5 \cdot (V_{\text{disp}} - V_{\text{cl}}) \quad (4)$$

where  $V_{\text{disp}}$  is the cylinders' volume, and  $V_{\text{cl}}$  is the clearance volume of the cylinder. The work performed by the cylinder gas on the piston during intake is

$$W_{\text{intake}} = p_1 \cdot (V_{\text{disp}} - V_{\text{cl}}) \quad (5)$$

The overall pressure losses during the intake and exhaust (pumping gas) in the ICE thermodynamic cycle are calculated using

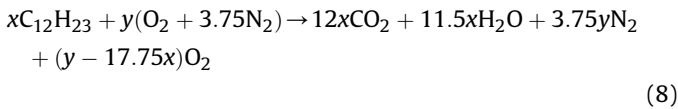
$$\Delta p_{\text{pump}} = p_1 - p_5 \quad (6)$$

The next expression represents the constant-volume combustion stage (2) and (3)

$$p_3 = \frac{M_a \cdot R_a}{M_g \cdot R_g} \cdot p_2 \cdot \frac{T_3}{T_2} = \frac{M_a \cdot R_a}{M_g \cdot R_g} \cdot p_2 \cdot \gamma \quad (7)$$

where  $\gamma$  is the temperature ratio of the constant-volume combustion stage.

For the combustion process in the cylinders, the average chemical formula for common diesel fuel is denoted as  $C_{12}H_{23}$  [24]. Therefore, the combustion process of diesel with air in the cylinders can be expressed simply as



where  $x$  is the molar flow rate of the diesel, and  $y$  is the molar flow rate of the intake air. The molar flow rate of air and diesel are calculated using

$$y = \frac{m_a}{M_a} \quad (9)$$

$$x = \frac{m_{\text{fuel}}}{M_{\text{fuel}}} \quad (10)$$

$$m_g = m_a + m_{\text{fuel}} \quad (11)$$

The energy balance during the combustion stroke (2–4) is expressed as

$$m_g \cdot c_{p_g} \cdot (T_4 - T_2) + \frac{W_{\text{combustion}}}{\tau} \cdot n = m_{\text{fuel}} \cdot q_{\text{LHV}} = Q \quad (12)$$

where  $q_{\text{LHV}}$  is the low heating value of the diesel, 44,000 kJ/kg [25].  $n$  represents the engine rotational speed in revolutions per unit

time and  $\tau$  represents the number of crank revolutions of each power stroke in the cycle.

The work performed during an isobaric combustion process (3–4) is calculated by

$$W_{\text{combustion}} = p_3 \cdot (V_4 - V_{\text{cl}}) \quad (13)$$

The work performed by the cylinder gas during the expansion stroke (4–5) is

$$W_{\text{expansion}} = \rho_i \cdot V_{\text{disp}} \cdot c_{p_g} \cdot T_4 \cdot \left( 1 - \beta^{\frac{k_g-1}{k_g}} \right) \cdot \eta_{\text{expansion}} \quad (14)$$

where  $\beta$  is the expand ratio of the cylinder gas during the isentropic expansion process. Its calculation can be performed using

$$\beta = \frac{p_5}{p_4} \quad (15)$$

The power and torque of the engine are the parameters of particular interest when matching an engine to a desired load. These two parameters can be determined given the  $p_{\text{MEP}}$  and  $V_{\text{disp}}$  of an engine. Because the power is simply the product of the torque and speed, only the analysis for the power is presented here. The formal definition of power equals work per unit time yielded

$$P_{\text{ICE}} = \frac{W_{\text{net}} \cdot n}{\tau} \quad (16)$$

Combined with Eq. (1), Eq. (16) can be expressed as

$$P_{\text{ICE}} = \frac{p_{\text{MEP}} \cdot V_{\text{disp}} \cdot n}{\tau} \quad (17)$$

For a two-stroke cycle,  $\tau$  is 1 and for a four-stroke cycle,  $\tau$  is 2. This term  $\tau$  is introduced by Heywood [23] to account for the number of crankshaft revolutions per power stroke.

The speed is calculated using the following expression:

$$n = \frac{n_0 \cdot m_a}{m_{a0}} \quad (18)$$

where  $m_{a0}$  and  $n_0$  are the intake air flow rate and revolution speed of the engine at rated load, respectively.

### 3.3.2. The turbocharger model

For the turbocharger used in the standalone ICE system or the ICE subsystem of the cascaded CPS model, the power output of the turbine is calculated using

$$P_{\text{itb}} = m_g \cdot c_{p_g} \cdot T_5 \cdot \left( 1 - \left( \frac{p_6}{p_5} \right)^{\frac{k_g-1}{k_g}} \right) \cdot \eta_{\text{itb}} \quad (19)$$

and its compression power consumption by the compressor of the turbocharger is expressed as

$$P_{\text{com}} = m_a \cdot c_{p_a} \cdot T_0 \cdot \left( \left( \frac{p_1}{p_0} \right)^{\frac{k_a-1}{k_a}} - 1 \right) / \eta_{\text{com}} = P_{\text{itb}} \quad (20)$$

For the turbocharger used in the ICE subsystem of the integrated CPS model, the power output of the turbine is calculated using



$$P_{itb} = m_g \cdot c_{p,g} \cdot T_5 \cdot \left( 1 - \left( \frac{p'_6}{p'_5} \right)^{\frac{k_g-1}{k_g}} \right) \cdot \eta_{itb} \quad (21)$$

The compression power consumption supplied by the turbo-charger in the integrated CPS model is expressed as

$$P_{com} = m_a \cdot c_{p,a} \cdot T_0 \cdot \left( \left( \frac{p'_1}{p_0} \right)^{\frac{k_g-1}{k_g}} - 1 \right) / \eta_{com} = P_{itb} \quad (22)$$

The waste heat recovered by the evaporator in the cascaded CPS model is expressed as

$$Q_2 = m_g \cdot c_{p,g} \cdot (T_6 - T_7) \quad (23)$$

where  $T_7$  is calculated according to the actual heat-transfer capacity of the evaporator.

The waste heat recovered by the evaporator in the integrated CPS model is expressed as

$$Q_2 = m_g \cdot c_{p,g} \cdot (T'_6 - T_7) \quad (24)$$

The thermal efficiency of the ICE subsystem is calculated using

$$\eta_{ICE} = P_{ICE} / Q_1 \cdot 100\% \quad (25)$$

### 3.4. The ORC subsystem model

#### 3.4.1. The evaporator model

For the waste heat recovery process in the ORC subsystem, a horizontal countercurrent shell-tube heat exchanger is used as the evaporator, and its energy balance during the heat-transfer process can be expressed as

$$Q_2 = h_{tot} \cdot A \cdot \Delta T_{LMTD} \quad (26)$$

The log mean temperature difference,  $\Delta T_{LMTD}$ , in the evaporator is calculated using

$$\Delta T_{LMTD} = \frac{(T_6 - T_{11}) - (T_7 - T_{10})}{\ln \frac{(T_6 - T_{11})}{(T_7 - T_{10})}} \quad (27)$$

The overall heat-transfer coefficient in the evaporator is expressed as

$$h_{tot} = \frac{1}{\frac{d_o}{d_i} \left( \frac{1}{h_t} + R_t \right) + R_s + \frac{d_o}{2\lambda_t} \ln \frac{d_o}{d_i} + \frac{1}{h_s}} \quad (28)$$

where  $h_s$  is the convective heat-transfer coefficient of the hot exhaust gas given in W/(m K),  $h_t$  is the heat-transfer coefficient of the organic working fluid given in W/(m K),  $d_i$  is the inner diameter of the tube, and  $\lambda_t$  is the conductive coefficient of the tube wall given in W/(m K). The fouling resistance on the tube-side and shell-side are calculated in this study:  $R_t$  is  $1.76 \times 10^{-4} \text{ m}^2 \text{ K/W}$ , and  $R_s$  is  $1.761 \times 10^{-3} \text{ m}^2 \text{ K/W}$ .

For the organic working fluid flow through the tube-side, its convective heat-transfer coefficient,  $h_t$ , is given by the following correlation [26]:

$$h_t = \frac{1.86(\text{Re}_t \cdot \text{Pr}_t \cdot d_i / l_t)^{1/3} \cdot \varphi \cdot \lambda_t}{d_i}, \quad \varphi = \left( \frac{\mu_t}{\mu_{t,m}} \right)^{0.14} \quad (29)$$

where  $\mu_{t,m}$  is the average dynamic viscosity of the working fluid through tube-side.

The liquid–gas phase change heat-transfer coefficient is calculated using [27]:

$$h_t = \frac{\lambda_v}{d_i} \frac{f_i/2 \cdot (\text{Re}_t - 1000) \cdot \text{Pr}_v}{1.0 + 12.7 \cdot (f_i/2)^{0.5} \cdot (\text{Pr}_v^{2/3} - 1)} \quad (30)$$

where  $f_i$  is the interfacial friction factor.

The shell-side convection heat-transfer coefficient is calculated using

$$h_s = j_c \cdot j_l \cdot j_b \cdot j_s \cdot j_{id} \cdot c_{p,g} \cdot \left( \frac{\dot{m}_g}{A_{cross}} \right) \cdot \left( \frac{\lambda_s}{c_{p,g} \cdot \mu_s} \right)^{2/3} \cdot \left( \frac{\mu_s}{\mu_{s,m}} \right)^{0.14} \quad (31)$$

All of the correction factors are available in [28].  $\mu_{s,m}$  is the average dynamic viscosity of the working fluid on the shell-side.

Only the pressure drop on the hot shell-side is calculated in this study, and the pressure drop of shell-tube heat exchangers consisting plain circulator tubes is given by

$$\Delta p_s = \frac{\text{fr} \cdot (m_g / A_{cross}) \cdot (N_b + 1) \cdot d_s}{2\rho_s \cdot d_{eq} \cdot \varphi}, \quad \varphi = \left( \frac{\mu_s}{\mu_{s,m}} \right)^{0.14} \quad (32)$$

where  $\text{fr}$  is the friction coefficient for the shell and  $\varphi$  is the viscosity correction fraction.

$$\text{fr} = \exp(0.576 - 0.19 \ln \text{Re}_s) \quad (33)$$

The Reynolds number on the shell-side,  $\text{Re}_s$  is provided by

$$\text{Re}_s = \frac{(m_g / A_{cross}) \cdot d_{eq}}{\mu_s} \quad (34)$$

For the triangular pitch layout studied in this paper, the equivalent diameter on the shell-side is calculated by

$$d_{eq} = \frac{4 \left( \frac{(l_{pit})^2 \sqrt{3}}{4} - \frac{\pi d_o^2}{8} \right)}{\frac{\pi d_o}{2}} + \frac{4(\pi/4)(d_s^2 - d_{t,o}^2)}{\frac{\pi d_o}{2} N_b} \quad (35)$$

The power output of the turbine is calculated using

$$P_{t,ORC} = \frac{1}{\eta_t} \cdot m_R \cdot c_{p,R} \cdot T_{11} \left[ 1 - (p_{12}/p_{11})^{\frac{\gamma-1}{\gamma}} \right] \quad (36)$$

where  $\eta_t$  is the isentropic efficiency of the turbine.

The following equation is used to model the turbine isentropic efficiency at different loads.

$$\eta_t = \eta_{to} \cdot \left( \frac{V_R}{V_{R0}} \right)^{0.5} \quad (37)$$

where  $\eta_{to}$  refers to the isentropic efficiency of the turbine at maximum load,  $V_R$  is the volume flow rate of the turbine, and  $V_{R0}$  refers the maximum volume flow rate of the turbine.

### 3.4.2. Other components' models

For the heat regenerator in the ORC subsystem, the mass flow rate on the hot-side and the cold-side are equivalent; thus, the energy balance equation is shown as

$$h_{10} - h_9 = h_{12} - h_{13} \quad (38)$$

For condenser in the ORC subsystem, its energy balance is expressed by

$$Q_4 = m_c \cdot c_{p,cf} \cdot \Delta T_{cf} = m_R \cdot (h_{13} - h_8) \quad (39)$$

in which  $\Delta T_{cf}$  is the temperature difference between the inlet and outlet on the cold-side (K), and  $c_{p,cf}$  is the specific heat capacity of the cooling fluid at constant pressure.

The power output of the ORC subsystem is calculated using

$$P_{ORC} = m_R \cdot w_{ORC} = P_{t,ORC} - P_{p,ORC} \quad (40)$$

where  $P_{p,ORC}$  is the power consumption of the pump. It is calculated using

$$P_{p,ORC} = m_R \cdot (h_9 - h_8) / \eta_p \quad (41)$$

The exergy efficiency of the evaporator is calculated using

$$\eta_{ex} = \frac{E_{x11} - E_{x10}}{E_{x6} - E_{x7}} 100\% \quad (42)$$

### 3.5. The overall performance index

The calculation formula for the thermal efficiency of the ICE subsystem is given as

$$\eta_{ICE} = \frac{P_{ICE}}{Q_1} 100\% = \frac{P_{ICE}}{Q_{1c} + Q_{1p}} 100\% \quad (43)$$

The thermal efficiency of the ORC subsystem is shown as

$$\eta_{ORC} = \frac{P_{ORC}}{m_g \cdot (h_6 - h_7)} 100\% \quad (44)$$

The overall power output of the ICE-ORC CPS is calculated using

$$P_{CPS} = P_{ICE} + P_{ORC} \quad (45)$$

The overall thermal efficiency of the ICE-ORC CPS is given as

$$\eta_{CPS} = \frac{P_{CPS}}{Q_1} 100\% \quad (46)$$

The improvement in the overall thermal efficiency of the ICE-ORC CPS is given as

$$\Delta \eta_{CPS} = \frac{\eta_{CPS} - \eta_{ICE}}{\eta_{ICE}} 100\% \quad (47)$$

## 4. Results and discussion

### 4.1. The operational parameter

To obtain the energy balance in an ICE, the experimental data from a commercial ICE (a 3516CDITA diesel engine) is used for the inputs for the topping ICE model. A steady-state analysis is carried out on this commercial engine, whose main operational parameters are listed in Table 1 [19]. The ambient temperature  $T_0$  is 288 K, and the ambient pressure  $p_0$  is 101 kPa.

**Table 1**

The operational parameters of the diesel engine model.

Model of engine	3516CDITA	Number of cylinders $N_c$	16
Engine rated power	2000	Clearance $V_{cl}$ , m <sup>3</sup>	0.0062
$P_{ICE}$ , kW			
Bore $B$ , mm	170	Rated air flow rate $m_{a0}$ , kg/s	3.88
Stroke $S$ , mm	190	Fuel flow rate $m_{fuel}$ , kg/s	0.113
Fuel lower heating value $q_{LHV}$ , MJ/kg	44	Number of crank revolutions $\tau$	2
Intake pressure $p_1$ , kPa	370	Specific heat ratio of the exhaust gas $k_g$	1.36
$\eta_{expansion}$	0.9	Specific heat ratio of air $k_a$	1.27
Mean effective pressure $p_{MEP}$ , kPa	2120	After intercooler temperature $T_i$ , K	323
$\eta_{compression}$	0.88	$c_{p,a}$ , kJ/(kg K)	1.06
Speed $n_0$ , RPS	30	$c_{p,g}$ , kJ/(kg K)	1.10
Exhaust gas temperature $T_6$ , K	735	$c_{p,R}$ , kJ/(kg K)	1.48

The structural parameters of the evaporator are presented in Table 2.

The following calculations are used to determine the size of the shell-tube heat exchanger.

First, a size of a shell-tube heat exchanger is guessed; Second, the ideal cross-flow heat-transfer coefficient is calculated according to the estimated size of the shell-tube heat exchanger; Third, the actual shell-side heat-transfer coefficient is calculated based on the appropriate correction factors; Finally, the size of the shell-tube heat exchanger is adjusted until the temperature requirements of the exhaust gas are met.

The saturated evaporation temperature of the organic working fluid in the evaporator is set to be no less than 473 K to prevent the exhaust gas from reaching the dew point in the evaporator. The vaporizing pressure of dichlorotrifluoroethane in the evaporator is set to 2500 kPa, and the isentropic efficiency of the turbine ( $\eta_{to}$ ) is set to 0.75. The isentropic efficiency of the pump ( $\eta_p$ ) is set to 0.75, the cooling fluid inlet temperature at condensation is 298 K, the average temperature difference of  $\Delta T_{cf}$  in condenser is set to 10 K, and the temperature increase of the cold organic working fluid in the preheater is set to 20 K.

### 4.2. Model verification

Figs. 3 and 4 show the relationship between  $P_{ICE}$  and  $\eta_{ICE}$  of the standalone ICE system and  $m_a$  (the intake air flow rate, IAF). The results are obtained based on the experimental data from a commercial CAT3516CDITA engine at different loads [19]. As can be observed from the two figures, the calculated data matches the experimental data well at the different IAFs. The maximum error in the calculation of the thermal efficiency is 9% at an air flow rate of 2.4 kg/s. Moreover, as can also be observed from Figs. 3 and 4, when

**Table 2**

The operational parameters of the evaporator model.

Parameter	Value	Parameter	Value
Tube inside diameter $d_i$ , mm	20	$z$	1.73
Tube outside diameter $d_o$ , mm	22.6	$\lambda_s$ , W/(m K)	0.0494
Tube length $l_t$ , mm	1,873	$j_c$	1
Tube pitch $l_{pit}$ , mm	38	$j_i$	0.75
Tube passes $t_{ps}$	4	$j_b$	0.8
Tube pattern $t_{pt}$	30 – triangular	$j_s$	0.9
Shell inside diameter $d_s$ , mm	710	$j_{id}$	1
Shell outside diameter $d_{so}$ , mm	726	$f_i$	1
Spacing at the inlet $S_i$ , mm	674.5	$Pr_t$	3.42
Baffle space $B_s$ , mm	500	$Pr_v$	1.24
Baffle cut $B_c$ , %	30	$\lambda_v$ , W/(m K)	0.0217
Number of baffle $N_{ob}$	2	$\lambda_t$ , W/(m K)	0.0810



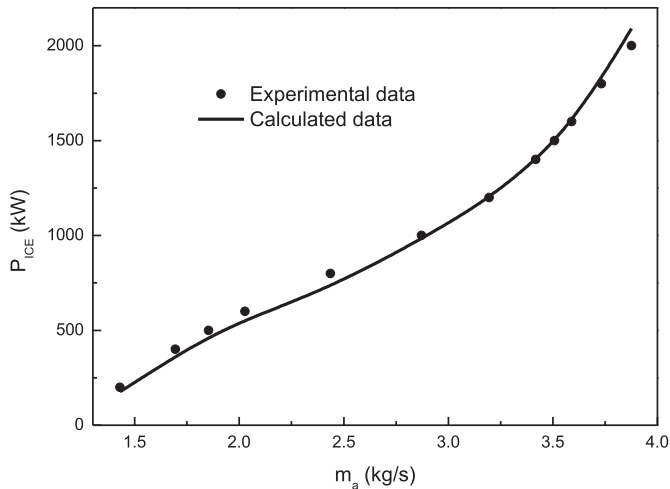


Fig. 3. The relationship between  $P_{ICE}$  and  $m_a$ .

the IAF is less than 3.2 kg/s, the power output and the thermal efficiency of the ICE steadily increase as the IAF increases, the power output of the ICE increases significantly as the IAF increases when the IAF is greater than 3.2 kg/s.

#### 4.3. The overall thermodynamic performance

Table 3 shows the thermodynamic performance of the ICE-ORC CPS. It is apparent from Table 3 that the overall power output of the system can reach 2365 kW, and the thermal efficiency of the CPS is of 44.9% in the cascaded ICE-ORC model, a 13.4% improvement in the overall thermal efficiency of the cascaded CPS model compared with the standalone ICE power system. The thermodynamic performance advantages of the cascaded ICE-ORC CPS as due to the substantial power output of the ORC subsystem and have only been considered in ideal form (i.e., a cascaded waste heat conversion unit); its practical influence on the ICE subsystem have not been calculated.

It can also be observed from Table 3 that, in the integrated CPS model, the pressure drop on the exhaust gas side is 14.7 kPa during the collection of the waste heat in the evaporator. To overcome the pressure loss and smoothly discharge the exhaust gas into the

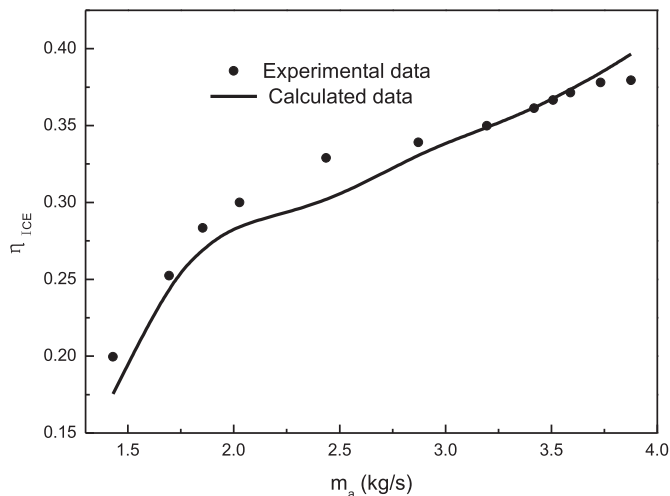


Fig. 4. The relationship between  $\eta_{ICE}$  and  $m_a$ .

Table 3

The thermodynamic performance of the ICE-ORC CPS.

Thermal performance index	Integrated <sup>a</sup>	Cascaded <sup>b</sup>
<b>ICE subsystem</b>		
Exhaust gas flow rate $m_g$ , kg/s	3.99	3.99
Exhaust temperature $T_6$ , K	735	712
Mean effective pressure $p_{MEP}$ , kPa	2020	2120
Power output of the ICE $P_{ICE}$ , kW	1982	2090
Thermal efficiency of the ICE subsystem $\eta_{ICE}$ , %	37.6	39.6
<b>ORC subsystem</b>		
Effective heat-transfer area of the evaporator $A$ , m <sup>2</sup>	30	30
Mass flow rate of dichlorotrifluoroethane $m_R$ , kg/s	3.0	2.9
Evaporation pressure of dichlorotrifluoroethane $p_{11}$ , kPa	2500	2500
Evaporator outlet temperature of dichlorotrifluoroethane $T_{12}$ , K	406	406
Evaporator outlet temperature of the exhaust gas $T_7$ , K	448	442
The log mean temperature difference in the evaporator $\Delta T_{LMTD}$ , K	202	189
Convective heat-transfer coefficient on the exhaust gas side of the evaporator $h_s$ , kW/(m <sup>2</sup> K)	0.242	0.243
Convective heat-transfer coefficient on the tube-side of the evaporator $h_t$ , kW/(m <sup>2</sup> K)	1.51	1.42
Over heat-transfer coefficient in the evaporator $h_{tot}$ , kW/(m <sup>2</sup> K)	0.207	0.207
Heat exchanged in the evaporator $Q_2$ , kW	1260	1180
Pressure drop on the exhaust gas side of the evaporator $\Delta p_s$ , kPa	14.7	/
Exergy efficiency of the evaporator $\eta_{ex}$ , %	46.5	47.3
Power output of the ORC subsystem $P_{ORC}$ , kW	271	262
Thermal efficiency of the ORC subsystem $\eta_{ORC}$ , %	21.6	22.3
<b>Combined power system</b>		
Overall power output $P_{CPS}$ , kW	2253	2365
Overall thermal efficiency $\eta_{CPS}$ , %	42.7	44.9
Improvement in the overall thermal efficiency $\Delta\eta_{CPS}$ , %	7.8 <sup>c</sup>	13.4

<sup>a</sup> Refers to the integrated ICE-ORC CPS model considering the coupling influence of the ORC subsystem and the ICE subsystem.

<sup>b</sup> Refers to the ICE-ORC CPS model, where the ORC subsystem is simply used as the thermal energy superimposition unit without considering the influence of the bottoming ORC subsystem on the topping ICE subsystem.

<sup>c</sup> Refers to the improvement in the thermal efficiency compared with the standalone ICE system.

ambient air, the exhaust pressure of the engine increases. The corresponding  $p_{MEP}$  of the engine decreases, and the power output of the engine is 1982 kW, which is 108 kW lower than that of the standalone ICE power system. However, as the engine exhaust pressure increases, the exhaust temperature of  $T_6$  increases from 712 K to 735 K, which is helpful for increasing the waste heat recovery in the evaporator and the power output of the ORC subsystem. In this study, the waste heat recovered from the exhaust gas in the evaporator is 1260 kW. This value is approximately 80 kW greater than the cascaded CPS model. Additionally, the power output of the ORC subsystem reaches 271 kW. Combining the above two results, it shows that the decrease in the power output of the ICE subsystem overweighs the increase in the power output of the ORC subsystem. The overall power output of the integrated ICE-ORC CPS model is 2253 kW, a 7.8% improvement in the thermal efficiency of the integrated CPS system model compared with the standalone ICE power system. That is, the overall thermal efficiency of the integrated CPS model is approximately 5.4 percentage points lower than that of the cascaded CPS model.

#### 4.4. The energy balance analysis

Fig. 5 shows the energy distribution of the integrated ICE-ORC CPS model. In addition to the useful power output from the ICE

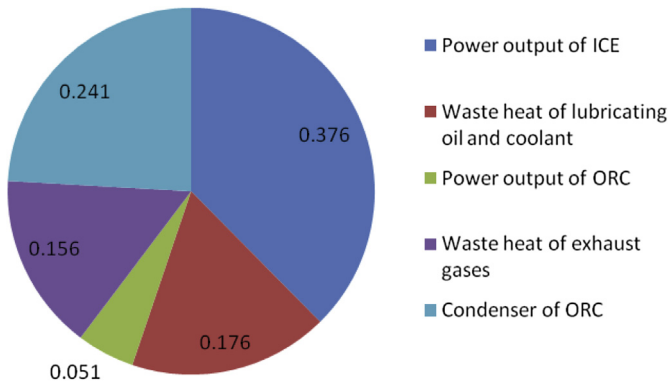


Fig. 5. The energy distribution of the integrated ICE-ORC CPS model.

and ORC subsystems, the energy loss in the condenser of the ORC subsystem is the largest; it accounts for 24.1% of the overall thermal energy input. The enthalpy loss in the exhaust gas is also large, and it accounts for approximately 15.6% of the overall thermal energy input. The waste heat removed by the ICE lubricating oil and the coolant is the lowest (approximately 17.6%).

Fig. 6 shows the exergy distribution of the integrated ICE-ORC CPS model used in this study. It is significantly different from the energy consumption distribution shown in Fig. 5. Even though there is no thermal energy loss in the evaporator, the high  $\Delta T_{LMTD}$  in the evaporator will cause a substantial exergy destruction, which accounts for approximately 16% of the overall fuel exergy input, while the exergy destruction in the condenser accounts for only 2.5%, due to its near ambient temperature and low  $\Delta T_{LMTD}$ . The exergy loss from the waste heat of the exhaust gas that discharges from the integrated CPS model is 16%. It can also be observed from Fig. 6 that the exergy in the engine exhaust gas is 32% of the overall fuel exergy input, but it is difficult to use effectively in the ORC subsystem. The main reasons are analysed in the following section.

It is assumed that reducing  $\Delta T_{LMTD}$  in the evaporator and the temperature of the exhaust gas exiting the evaporator are appropriate measures to improve the thermal efficiency of the ICE-ORC CPS considering the second law of thermodynamics. However, according to the calculated result in Table 3, the low heat-transfer coefficient on the exhaust gas side of the evaporator (approximately  $0.242 \text{ kW}/(\text{m}^2 \text{ K})$  at rated load) causes a low overall heat-transfer coefficient in the evaporator.  $\Delta T_{LMTD}$  is approximately 202 K, and its effective heat-transfer area reaches  $30 \text{ m}^2$ . When heat-transfer enhancement measures are taken to reduce  $\Delta T_{LMTD}$ , a larger effective heat-transfer area for the evaporator is needed, which will cause an increase in the size and cost of the evaporator.

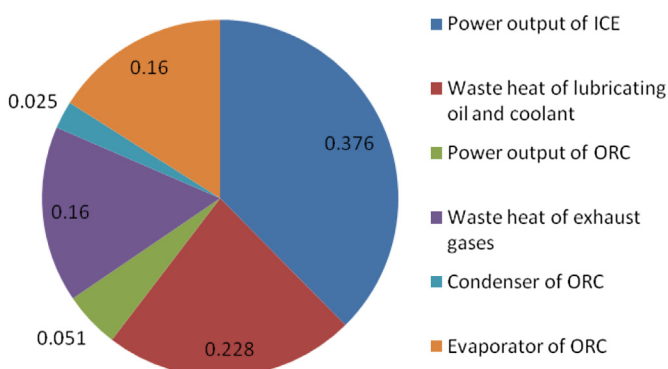


Fig. 6. The exergy distribution of the integrated ICE-ORC CPS model.

Furthermore, increasing the heat-transfer area would cause an increase in the pressure loss on the exhaust gas side of the evaporator, and the engine exhaust manifold temperature would increase correspondingly because a decrease in the power output of the ICE subsystem outweighs the increase in the power output of the ICE subsystem, compared with the cascaded CPS model. Therefore, either the overall power output or the thermal efficiency of the integrated CPS model decrease significantly compared with the cascaded CPS model. However, the cost of the evaporator would be significantly increased due to the low heat-transfer coefficient. Therefore, despite the exergy loss on the exhaust gas side in evaporator is 16%, it is uneconomical to improve its thermal performance by the continuously recovering the waste heat from the exhaust gas. Lowering the temperature of the exhaust gas exiting the evaporator is not feasible. It will cause equipment corrosion when the temperature of the exhaust gas exiting the evaporator is too low or near its dew point.

#### 4.5. The impact of the IAF

Fig. 7 shows the relationship between the exhausts gas pressure drop, the overall heat-transfer coefficient of the evaporator and the IAF in the integrated CPS model. As shown, both the pressure drop on the hot exhaust gas side and the overall heat-transfer coefficient of the evaporator decrease as the IAF decreases. Generally, the extent of the pressure drop on the exhaust gas side of the evaporator is reduced from 14.7 kPa to 1.53 kPa and the overall heat-transfer coefficient of the evaporator decreases from  $0.207 \text{ kW}/(\text{m}^2 \text{ K})$  to  $0.093 \text{ kW}/(\text{m}^2 \text{ K})$  when the IAF declines from 3.88 kg/s to 1.43 kg/s. It can be observed from Fig. 7 that the overall heat-transfer coefficient of the evaporator increases nearly linear with increasing IAF, which is directly caused by the heat-transfer resistance on the exhaust gas side of the evaporator and is much higher than that on the organic working fluids side of the evaporator. This behaviour determines the overall heat-transfer coefficient of the evaporator. The heat-transfer coefficient on the hot exhaust gas side increases linear as the IAF increase according to Eq. (31). It can also be observed from Fig. 7 that the pressure drop on the exhaust gas side increases nearly exponentially with increasing IAF. The reason can be explained by the flow conditions on the exhaust side, which are mainly affected by the friction coefficients and the IFA. The pressure drop increases linearly with the IFA for a given friction coefficient, while the friction coefficient of the pressure drop increases exponentially with the IFA (according to Eqs. (32)–(34)).

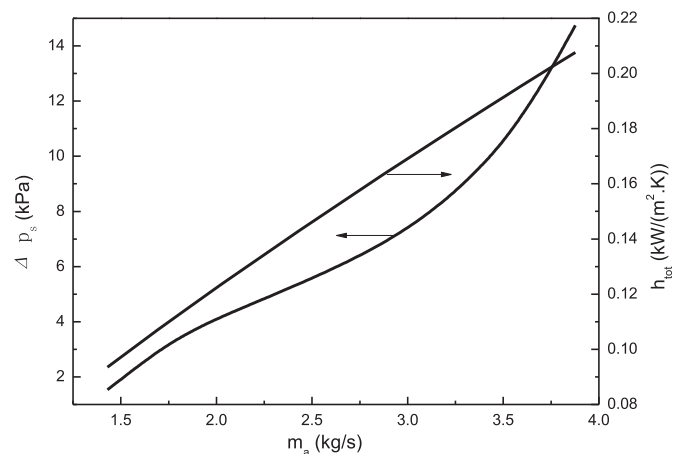
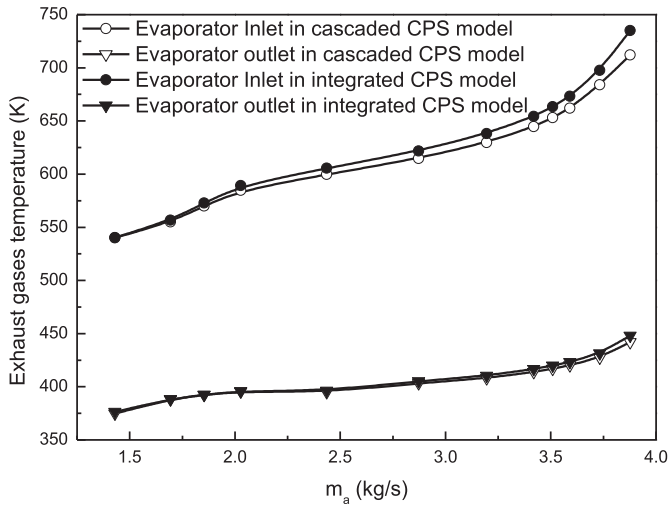


Fig. 7. The relationship between  $\Delta p_s$ ,  $h_{tot}$  and  $m_a$  in the integrated CPS model.



**Fig. 8.** The relationship between the exhaust gas temperature exiting evaporator and  $m_a$ .

Therefore, the pressure drop on the exhaust gas side increases substantially as the IAF increases.

Fig. 8 shows the relationship between the exhaust gas temperature through the evaporator and the IAF. It is evident that both the inlet and outlet temperatures of the exhaust gas through the evaporator in the integrated CPS model are higher than those of the cascaded CPS model. The corresponding temperature difference between the inlet and outlet on the exhaust gas side of the evaporator increases as the IAF increases in both CPS models. Moreover, it can also be observed that, when the IAF is lower than 2.5 kg/s, the temperature of the exhaust gas exiting the evaporator will be lower than 400 K, which is near the minimum allowed temperature of the exhaust gas [15]. As the IAF continues to decrease, the temperature of the exhaust gas exiting the evaporator is near or below its dew point, which will cause corrosion problems in the subsequent components.

Figs. 9 and 10 show the relationship between the power output and the thermal efficiencies of the ICE and IAF, respectively. Both the power output and thermal efficiency of the ICE increase with increasing IAF. However, the extent of the decrease in integrated CPS model is more significantly than in the standalone ICE system

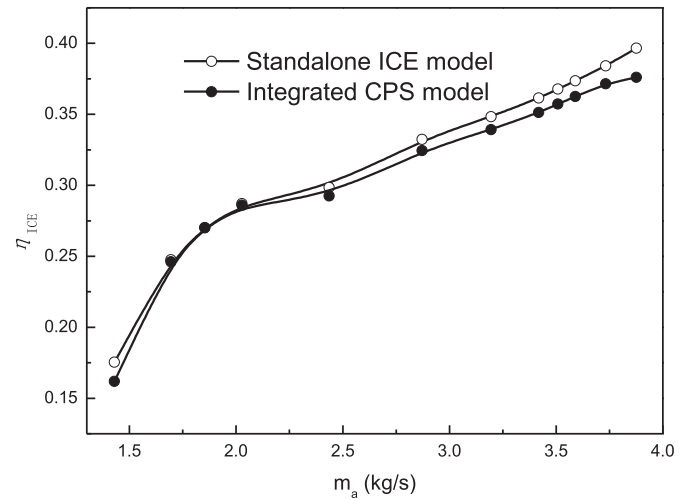


**Fig. 10.** The relationship between  $\eta_{ICE}$  and  $m_a$ .

model, which can be explained by interpreting Fig. 7: the pressure drop on the exhaust gas side of the evaporator increases as the IAF increases, which causes a decrease in the  $p_{MEP}$  and the decrease of the net work of the ICE subsystem in the integrated CPS model. Therefore, the decreases of the engine power output and thermal efficiency in the integrated CPS model are more evident than in the standalone ICE model. As shown in Figs. 9 and 10, the power output of the ICE subsystem decreases by 108 kW, a 2.0% decrease in the thermal efficiency of the ICE subsystem compared with the standalone ICE system model, when the IAF is 3.88 kg/s.

Fig. 11 shows the relationship between the thermal efficiency of the ORC subsystem and the IAF. The integration of the bottoming ORC subsystem with the topping ICE subsystem causes a decrease in the thermal efficiency of the ORC subsystem in the integrated CPS model, and the thermal efficiency of the ORC subsystem in the integrated CPS model is always less than that of the cascaded CPS model for any IFA, while the extent of the increase in the thermal efficiency of the ORC subsystem between the models increases as the IAF increases, which can be explained by the fact that the integration process causes an increase in the engine exhaust manifold temperature; the waste heat recovered in the evaporator is greater in the integrated CPS model.

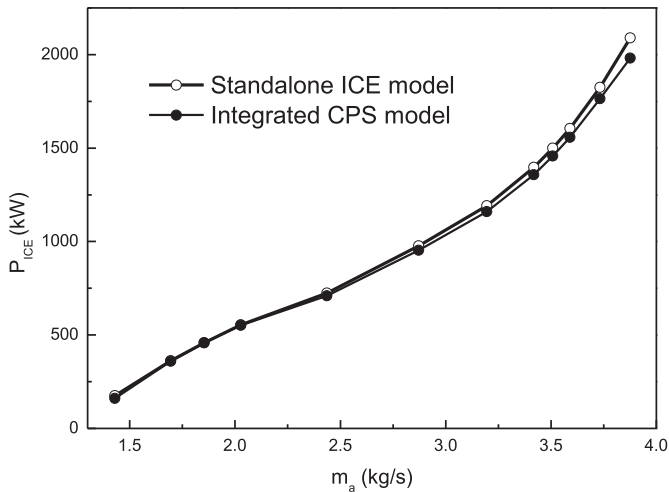


**Fig. 9.** The relationship between  $P_{ICE}$  and  $m_a$ .

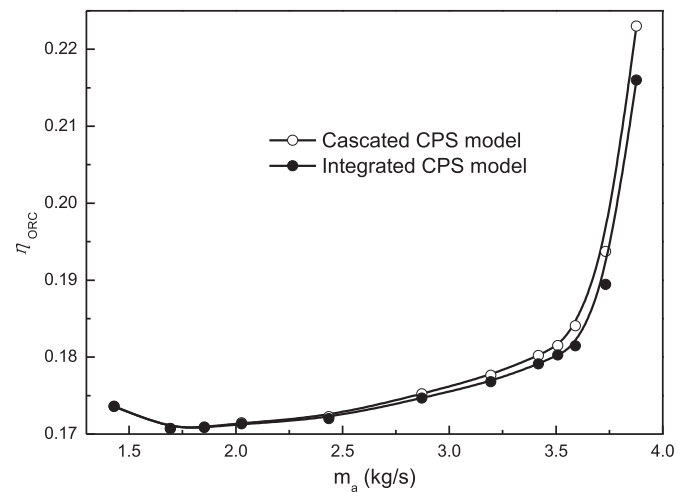


**Fig. 11.** The relationship between  $\eta_{ORC}$  and  $m_a$ .

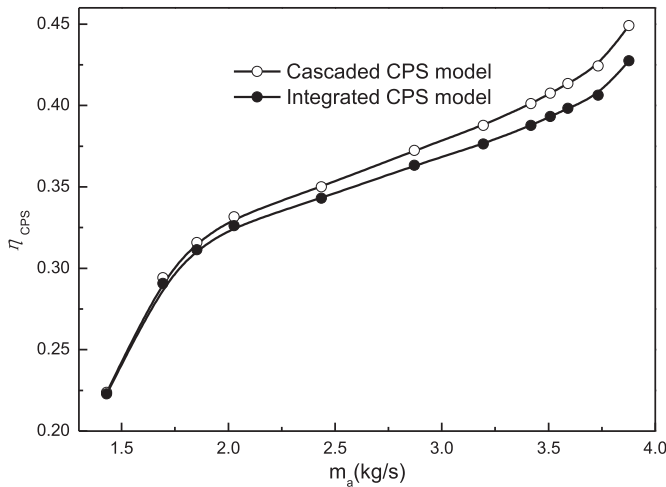


Fig. 12. The relationship between  $\eta_{CPS}$  and  $m_a$ .

Fig. 12 shows the relationship between the overall thermal efficiency and the IAF. This figure illustrates the integration of the ICE subsystem with the ORC subsystem, which causes the overall thermal efficiency of the integrated CPS model to always be less than that of the cascaded CPS model for any IAF because the decrease in the power output of the ICE subsystem outweighs the increase in the power output of the ORC subsystem in the integrated CPS model. However, this result demonstrates that integrating the bottoming ORC subsystem with the topping ICE subsystem significantly affects the overall thermal performance of the integrated CPS model as the IAF increases, which is due to the increase in the pressure drop of the exhaust gas and the decrease of  $p_{MEP}$  as the IAF increases. As a result, the decrease in the power output of the ICE and the increase in the power output of the ORC are both enhanced. Furthermore, in the integrated CPS model, the extent of the decrease of the thermal efficiency of the integrated CPS model also increases as the IAF increases.

#### 4.6. Sensitivity analysis of the evaporating pressure of the ORC subsystem

Fig. 13 shows the relationship between the waste heat recovered in the evaporator, the thermal efficiency of the ORC subsystem and the evaporating pressure (for the integrated CPS model). The results are for an IAF of 3.88 kg/s. It can be observed from Fig. 13 that the

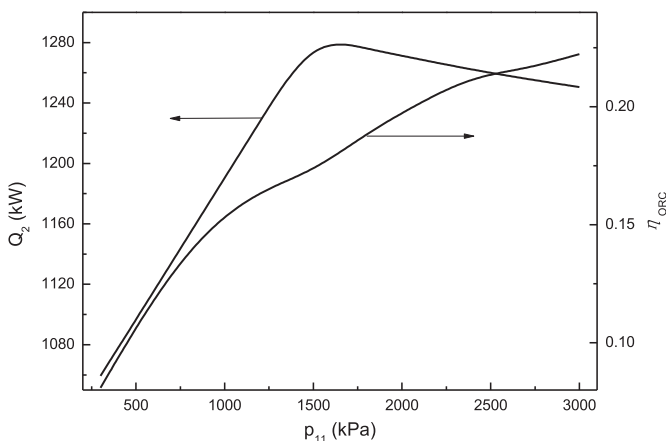


Fig. 13. The relationship between  $Q_2$ ,  $\eta_{ORC}$  and  $p_{11}$  (the integrated CPS model).

amount of low-grade waste heat that is recovered increases by only approximately 200 kW when the evaporating pressure increases from 300 kPa to 3000 kPa; the average thermal efficiency of the ORC subsystem is 20%, and it can be inferred that the power output of the ORC subsystem increases by approximately 40 kW. Combined with the results shown in Fig. 9, the power output of the ICE subsystem decreases by 108 kW, considering the exhaust gas pressure drop of 14.7 kPa on the exhaust gas side of the evaporator, which illustrates that the influence of the evaporating pressure on the cold organic working fluid side on the waste heat recovery efficiency is much less than the pressure drop on the exhaust gas side of the evaporator.

Moreover, it can also be observed from Fig. 13 that there exists a maximum waste heat recovery when the evaporating pressure increases from 300 kPa to 3000 kPa, which can be explained by the heat-transfer coefficient on the hot exhaust gas side of the evaporator and includes the convective heat-transfer and liquid-to-gas phase change heat-transfer. The convective heat-transfer coefficient is lower than that of phase change heat-transfer coefficient. The heat transferred by convection increases, and the phase change heat-transfer decreases as the evaporating pressure increases. However, the heat-transfer coefficient at cold organic working fluid side of the evaporator is higher than on the exhaust gas side, and the change in the heat-transfer coefficient caused by the flow conditions on the cold working fluids side affects the overall heat-transfer coefficient of the evaporator less than the exhaust gas side. Therefore, the pressure drop on the cold, organic working fluids side in the evaporator is omitted, and only the influence of the pressure drop on the exhaust gas side of the evaporator on the integrated performances of the ICE-ORC CPS is analysed in this study.

## 5. Conclusions

Two thermodynamic calculation models for the same ICE-ORC CPS system are developed based on the experimental performance data of a commercial engine, and the integrated performance of the ICE-ORC CPS is studied. In the integrated CPS model, the ORC subsystem does more with the waste heat collected from the ICE exhaust gas than the cascaded collection. Additionally, the impact on the operational performance of the engine and the integrated performance of the CPS are analysed by comparing the two calculation models in this paper. The following conclusions are drawn.

- (1) The integration of the bottoming ORC subsystem with the topping ICE subsystem improves the thermal efficiency of the bottoming ORC subsystem but significantly reduces the thermal efficiency of the topping ICE subsystem. Considering the influence of the pressure drop through the waste heat recovery evaporator on the exhaust gas side of the topping ICE, the thermal efficiency of the ICE-ORC CPS is improved by 7.8% compared with the standalone ICE system, but the thermal efficiency of the ICE subsystem decreases by 2.0% compared with the standalone ICE system (all values reported for an engine rated IAF of 3.88 kg/s) in the integrated CPS model.
- (2) Matching the pressure drop and heat-transfer in the evaporator causes a decrease in the power output of the ICE subsystem; nonetheless it outweighs the corresponding increase in the power output of the ORC subsystem in the integrated CPS model. In addition, the coupling process significantly affects the overall thermal performance as the IAF increases compared with the cascaded CPS model. The power output of the ICE subsystem decreases from 2090 kW to 1982 kW, and



the power output of the ORC subsystem increases by approximately 9 kW; the overall power output of the CPS model decreases by 112 kW compared with the cascaded CPS model at the engine rated load.

- (3) The coupling of the fluid flow and heat-transfer in the evaporator causes a clear decreasing in the temperature of the exhaust gas exiting the evaporator. When the IAF does not exceed 2.5 kg/s, the temperature of the exhaust gas exiting the evaporator reaches its minimum. The temperature of the exhaust gas exiting the evaporator will be near or below its dew point, which might cause corrosion problems in the subsequent components as the IAF continues to decrease.

## Acknowledgements

The authors gratefully acknowledge the financial support provided by the Project Funded by the Priority Academic Program Development (PAPD) of the Jiangsu Higher Education Institutions and Project Funded by the Youth Natural Science Foundation of Jiangsu Province, China (Project No. BK20130799).

## Appendix A. Supplementary data

Supplementary data related to this article can be found at doi:10.1016/j.energy.2014.05.103.

## Appendix A1

**Table A1**

The input parameter for the diesel engine model.

Intake air flow rate $m_a$ (kg/s)	Air-fuel ratio (kg/kg)	$p_{MEP}$ (kPa)	Exhaust gas temperature $T_6$ (K)	Pressure exiting intercooler $p_1$ (kPa)	Temperature exiting intercooler $T_1'$ (K)
3.88	34.2	2120	712.0	367	323
3.73	36.5	1900	682.5	350	322
3.59	38.8	1700	659.5	332	321
3.51	39.9	1590	648.9	323	320
3.42	41.1	1490	638.4	313	320
3.19	43.4	1300	617.6	290	319
2.87	45.3	1100	596.0	259	318
2.43	46.6	903	568.7	220	317
2.03	48.8	703	535.1	183	317
1.85	50.6	607	514.4	168	317
1.69	53.7	503	490.6	154	316
1.43	66.4	296	419.2	131	316

## References

- [1] Peris B, Esbri JN, Francisco MF. Bottoming organic Rankine cycle configurations to increase internal combustion engines power output from cooling water waste heat recovery. *Appl Therm Eng* 2013;61:364–71.
- [2] Danov SN, Gupta AK. Modeling the performance characteristics of diesel engine based combined-cycle power plants – part I: mathematical model. *J Eng Gas Turb Power* 2004;126:28–34.
- [3] Danov SN, Gupta AK. Modeling the performance characteristics of diesel engine based combined-cycle power plants – part II: results and applications. *J Eng Gas Turb Power* 2004;126:35–43.
- [4] Yu C, Chau KT. Thermoelectric automotive waste heat energy recovery using maximum power point tracking. *Energy Convers Manage* 2009;50:1506–12.
- [5] Miller EW, Hendricks TJ, Peterson RB. Modeling energy recovery using thermoelectric conversion integrated with an organic Rankine bottoming cycle. *J Electr Mater* 2009;38:1206–13.
- [6] Yamada N, Mohamad MNA. Efficiency of hydrogen internal combustion engine combined with open steam Rankine cycle recovering water and waste heat. *Int J Hydrogen Energy* 2010;35:1430–42.
- [7] Kalyan KS, Pedra JM, Sundar RK. Analysis of exhaust waste heat recovery from a dual fuel low temperature combustion engine using an Organic Rankine Cycle. *Energy* 2010;35:2187–99.
- [8] Shu GP, Zhao J, Tian H, Liang XY, Wei HQ. Parametric and exergetic analysis of waste heat recovery system based on thermoelectric generator and organic rankine cycle utilizing R123. *Energy* 2012;45:806–16.
- [9] Vaja I, Gambarotta A. Internal combustion engine (ICE) bottoming with organic Rankine cycles (ORCs). *Energy* 2010;35(2):1084–93.
- [10] Fang JL, Wei MS, Wang RJ, Ma CC. Simulation of waste heat recovery from a heavy-duty diesel with a medium temperature ORC system. *Trans CSICE* 2010;28(4):362–7.
- [11] He MG, Zhang XX, Zeng K, Gao K. A combined thermodynamic cycle used for waste heat recovery of internal combustion engine. *Energy* 2011;36:6821–9.
- [12] Wang EH, Zhang HG, Zhao Y, Fan BY, Wu YT, Mu QH. Performance analysis of a novel system combining a dual loop organic Rankine cycle (ORC) with a gasoline engine. *Energy* 2012;43:385–95.
- [13] Domingues A, Santos H, Costa M. Analysis of vehicle exhaust waste heat recovery potential using a Rankine cycle. *Energy* 2013;49:71–85.
- [14] Stobart RK. An availability approach to thermal energy recovery in vehicles. *Proc Inst Mech Eng D* 2007;221:1107–24.
- [15] Tian H, Shu G, Wei H, Liang X, Liu L. Fluids and parameters optimization for the organic Rankine cycles (ORCs) used in exhaust heat recovery of internal combustion engine (ICE). *Energy* 2012;47:125–36.
- [16] Mavridou S, Mavropoulos GC, Bouris D, Hountalas DT, Bergeles G. Comparative design study of a diesel exhaust gas heat exchanger for truck applications with conventional and state of the art heat transfer enhancements. *Appl Therm Eng* 2010;30:935–47.
- [17] Han XH, Li P, Wang Z, Wang XH, Zhang XJ, Chen GM. Evaporation heat transfer and pressure drop of R161 in a 7mm micro-fin tube. *Int J Heat Mass Transfer* 2013;62:638–46.
- [18] Taylor AMKP. Science review of internal combustion engine. *Energy Policy* 2008;36:4657–67.
- [19] Yue C, Han D, Jiao WQ, Pu WH, Lu P. Technological and economic performance analysis for ICE-ORC compounded power system. *Trans CSICE* 2012;30(3):266–71 [in Chinese].
- [20] Roy JP, Misra A. Parametric optimization and performance analysis for a regenerative Organic Rankine Cycle using R123 for waste heat recovery. *Energy* 2012;39:227–35.
- [21] Lottin O, Epiard C. Dependence of the thermodynamic properties of ice slurries on the characteristics of marketed antifreezes. *Int J Refrigeration* 2001;24:455–67.
- [22] Hung TC. A review of organic rankine cycles (ORCs) for the recovery of low-grade waste heat. *Energy* 1997;22(7):661–7.
- [23] Heywood JB. Internal combustion engine fundamentals. New York, USA: McGraw-Hill; 1998.
- [24] Zhang HG, Wang EH, Fan BY. A performance analysis of a novel system of a dual loop bottoming organic Rankine cycle(ORC) with a light-duty diesel engine. *Appl Energy* 2013;102:1504–13.
- [25] Graboski MS, McCormick RL. Combustion of fat and vegetable oil derived fuels in diesel engines. *Prog Energy Combust Sci* 1998;24:125–64.
- [26] Bejan A, Kraus A. Heat transfer handbook. New Jersey, USA: Wiley & Sons; 2003.
- [27] Chiou CB, Lu DC, Wang CC. Analysis of evaporation of non-azeotropic refrigerants in a horizontal tube. *Appl Therm Eng* 1996;16(10):817–27.
- [28] Shah RK, Sekulic DP. Fundamentals of heat exchanger design. New Jersey, USA: Wiley & Sons; 2003.